Delivery report

PV-LAC

PROBA-V ATMOSPHERIC CORRECTION & COASTAL PRODUCTS

PV-LAC: Advanced Land, Aerosol and Coastal Products for PROBA-V

PV-LAC: D6-A2, Aerosol Optical Thickness and Surface Reflectance Validation Report v2

Erwin Wolters, Marta Luffarelli, Yves Govaerts, and Else Swinnen

January 2018

DISTRIBUTION LIST

Author(s)	:	Erwin Wolters, Marta Luffarelli, Yves Govaerts, and Else Swinnen
Reviewer(s)	:	Fabrizio Niro
Approver(s)	:	Fabrizio Niro
Issuing authority	:	VITO

CHANGE RECORD

Release	Date	Pages	Description of change	Editor(s)	Reviewer(s)
V1.0	3/05/2017	All	First version	E. Wolters, E. Swinnen, M. Luffarelli, and Y. Govaerts	Philippe Goryl, Fabrizio Niro
V2.0	3/10/2017	All	Additional validation results for CISAR v2 and incorporated review comments on VR v1 by F. Niro	E. Wolters, E. Swinnen	Fabrizio Niro
V2.1	27/10/2017	All	Incorporated review comments by R. Niro	E. Wolters, E. Swinnen	Fabrizio Niro
V2.2	8/1/2018	All	Added methodology, results, and summary/conclusions for BHR comparison of additional datasets (Meteosat-SEVIRI and PROBA-V S10 TOC) and modified TOC reflectance comparison, using the CISAR- and MODIS-retrieved RPV parameters.	E. Wolters, E. Swinnen	Fabrizio Niro

TABLE OF CONTENTS

LIST OF FIGURES

LIST OF TABLES

LIST OF ABBREVIATIONS AND ACRONYMS

AERONET	Aerosol Robotic Network
AOT	Aerosol Optical Thickness
ATBD	Algorithm Theoretical Basis Document
BHR	Bi-Hemispherical Reflectance
BRDF	Bidirectional Reflectance Distribution Function
BRF	Bi-directional Reflectance Factor
CISAR	Combined Inversion of Surface and AeRosols
ECHAM	ECMWF Hamburg Model
FWHM	Full Width at Half Maximum
GCOS	Global Climate Observing System
LSA-SAF	Land Surface Analysis Satellite Application Facility
MODIS	Moderate-Resolution Imaging Spectrometer
NIR	Near-Infrared
ODR	Orthogonal Distance Regression
PROBA-V	Project for On-Board Autonomy – Vegetation
QI	Quality Indicator
RPV	Rahman-Pinty-Verstraete BRDF model
SEVIRI	Spinning Enhanced Visible and Infrared Imager
SMAC	Simplified Model for Atmospheric Correction
SR	Surface Reflectance
SWIR	Short Wave Infrared
TOA	Top-of-Atmosphere
TOC	Top-of-Canopy

CHAPTER 1 INTRODUCTION

This document describes the Aerosol Optical Thickness (AOT) and Bi-Hemispherical Reflectance (BHR) validation, which are obtained from Project for On-Board Autonomy – Vegetation (PROBA-V) observations using the Combined Inversion of Surface and AeRosols (CISAR) algorithm (Govaerts and Luffarelli, 2017). A detailed algorithm description applied to the PROBA-V observations is given in the Algorithm Theoretical Baseline Document (ATBD, D2-A2).

The validation objectives are the following:

- To obtain an indication on the usefulness of applying CISAR to PROBA-V observations and on the method's performance
- To assess whether CISAR's performance is of added value compared to the current operationally retrieved AOT and TOC reflectance

The Validation Report is built up as follows. CHAPTER 2 explains the validation methodology, followed by the main results and their interpretation in CHAPTER 3. A discussion and summary are given in CHAPTER 4.

CHAPTER 2 VALIDATION METHODOLOGY

2.1. INTRODUCTION AND GENERAL METHODOLOGY

The validation of the CISAR algorithm is performed in two parts:

(1) validation of the retrieved AOT with collocated AERONET AOT observations over 50 globally distributed stations,

(2) validation of the derived BHR with corresponding MODIS BHR for the same 50 stations, and

(3) comparison of the CISAR's directional TOC reflectances with those retrieved from the current operational aerosol retrieval and atmospheric correction algorithm, as well as with a 'theoretical ground truth' TOC reflectance derived from temporally collocated AERONET AOT values. All validation was carried out for 2014 – 2015.

For both the AOT and BHR validation, statistical metrics to assess the method's performance are calculated. These metrics express the accuracy, precision, and (relative) uncertainty. Here, we have adopted the metrics introduced by Claverie et al. (2015), which are presented below.

- Accuracy (*A*):

$$A = \frac{1}{n}\sum_{i=1}^{n}\varepsilon_i$$

- Precision (*P*):

$$P = \sqrt{\frac{1}{n-1}\sum_{i=1}^{n}(\varepsilon_i - A)^2}$$

- Uncertainty (*U*):

$$U = \sqrt{\frac{1}{n}\sum_{i=1}^{n}{\varepsilon_i}^2}$$

- Relative uncertainty (*rU*):

$$rU = \frac{U}{\overline{m}}$$

In these equations, n is the number of valid samples used in the comparison, ε_i is the retrieved minus the reference value, and $\overline{m}$ denotes the average of the reference observations, being AERONET for AOT, MODIS Bi-Hemishperical Reflectance (BHR) for the retrieved CISAR BHR, and TOC reflectance obtained from PROBA-V geometries, TOA reflectances, and AERONET AOT data for

the TOC reflectance validation, respectively. For each of the performance metrics, a value close to zero indicates a good agreement with the reference dataset.

Additional to the above introduced performance metrics, a linear least square regression, taking into account the error in both the CISAR and AERONET/MODIS values, was performed. The linear regressions were calculated using the Orthogonal Distance Regression (ODR) package available in the Python `scipy` module.

The AOT and BHR validations were performed for all stations, as well as for the following subcategories: 'partly vegetated', 'fully vegetated', 'bare soil', and 'mixed surfaces'. For each AERONET station, Google Maps images of the area over which the AOT and BHR were retrieved were visually interpreted into one of the above categories. It is noted that the 'mixed surfaces' category mainly consists of urban areas mixed with some vegetation in the surroundings.

The modifications incorporated in CISAR v2 were the introduction of a Quality Indicator and aerosol layer height climatology data replacing the fixed 2 km aerosol layer height of v1. For both the AOT and BHR validation, results of CISAR v2 are compared with CISAR v1. In addition, the impact of the Quality Indicator introduced in CISAR v2 is assessed.

2.2. AOT VALIDATION METHODOLOGY

Validation of the CISAR AOT retrieval is performed through comparison with Aerosol Robotic Network (AERONET) Level 2.0 (cloud screened and quality assured) AOT. As the CISAR-retrieved AOT is representative for 0.55 µm, and knowing that AOT exponentially decreases with increasing wavelength, it is important to have AERONET AOT values available at the same wavelength. Because the AOT is not directly observed at 0.55 µm, an approximate value is obtained using the retrieved AOT at 0.44 µm (at some stations a slightly different wavelength of 0.443 µm is used) and the retrieved Ångström parameter (α) for the wavelengths 0.44 – 0.675 µm:

$$AOT_{0.55} = AOT_{0.44}\left(\frac{\lambda}{\lambda_o}\right)^{-\alpha}$$

With $AOT_{0.44}$ and α being the retrieved *AOT* at 0.44 µm and Ångström parameter, respectively.

To account for the difference in spatial representativeness between the CISAR retrieved AOT for a single 1 × 1 km^2 pixel and the AERONET AOT, the median of AERONET AOT values within +/- 30 minutes centered at the PROBA-V overpass times was calculated. Further, in order to assume a homogeneous ground-based aerosol distribution in the considered spatial area, the difference between the maximum and minimum AOT value relative to the median within the 1-hour time interval should be < 20%. This additional homogeneity criterion removed ~10% of the initially collected AERONET AOT retrievals. From the paired datasets, scatterplots were made and the statistical metrics introduced in section 2.1 were calculated for all stations aggregated, as well as for the subsets based on vegetation coverage. In addition, in order to assess whether CISAR is capable of capturing the temporal AOT evolution, time series for selected sites were made. Figure 1 shows the global distribution of the used AERONET stations. The stations were selected to obtain a good balance in terms of geographical and climatological spread, as well as different aerosol types. Initially, 99 stations fulfilling these criteria were selected. However, the final selection was reduced

to 50 stations as a result of amongst others insufficient AERONET AOT observations available, too limited or no CISAR retrievals due to low solar elevations, snow and/or cloud coverage, etc.

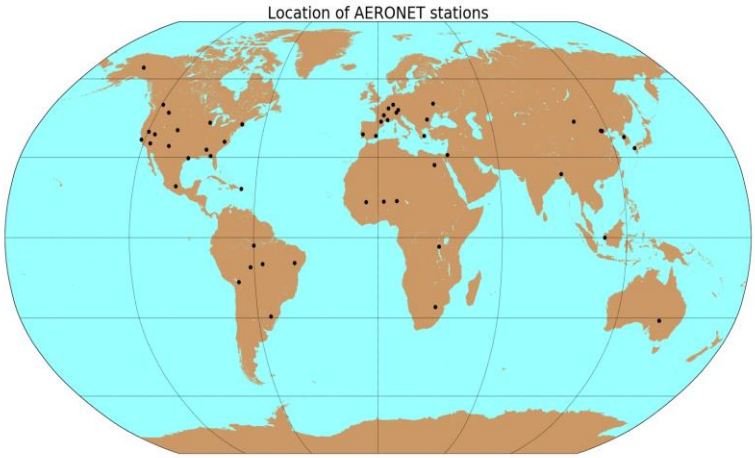

Figure 1: Global distribution of the AERONET stations used for the AOT validation.

2.3. SR REFLECTANCE VALIDATION METHODOLOGY

The Surface Reflectance (SR) validation was performed for the Bi-Hemispherical Reflectance (BHR) and directional TOC reflectance, which will be further highlighted below.

2.3.1. BI-HEMISPHERICAL REFLECTANCE VALIDATION

First, as the surface reflectance obtained from CISAR is delivered as BHR, *i.e.*, the reflectance one would measure under isotropic illumination conditions, a comparison with MODIS BHR data (MCD43A1 product, Collection 5 [Lucht et al., 2000]) was performed. This product provides BHR at 500 m resolution for observations accumulated over 16 days with an 8-day shift, assuming constant surface conditions. Although the temporal accumulation and window shift periods for CISAR and MODIS are similar, it is noted that differences between the CISAR and MODIS BHR can be expected due to some intrinsic instrumental and algorithmic differences.

- *Spectral differences:* the MODIS bands that spectrally correspond with PROBA-V are slightly displaced and are also narrower than the PROBA-V channels. The corresponding MODIS and PROBA-V spectral response functions are presented in Figure 2.

- *Aerosol retrieval and atmospheric correction differences:* MODIS uses a dark target technique (Levy et al., 2015) to retrieve aerosol information and uses the 6S (Vermote et al., 1997) radiative transfer model to perform the atmospheric correction. These differences could be subject of additional research, however, due to time constraints we cannot elaborate on the effects of these differences within this project.

- *Cloud detection difference:* although the modified PROBA-V cloud screening algorithm gives accurate results (Stelzer et al., 2016), differences in the obtained cloud-free datasets

for given periods and regions will occur due to MODIS' more extensive cloud detection capabilities. As the MODIS instrument observes in the spectral range 0.4 – 14.2 µm, cloud detection can be done more accurately than is possible for the four VNIR-SWIR PROBA-V spectral channels. MODIS benefits from additional thermal infrared and shortwave water vapor absorption channel observations, with the latter specifically designed for cirrus cloud detection. Frey et al. (2008) and Ackerman et al. (2008) provide detailed descriptions on the MODIS cloud detection algorithm and its validation.

- *BRDF model inversion difference:* the CISAR method uses the Rahman-Pinty-Verstraete (RPV, Rahman et al., 1993) model for BRDF inversion, while the MODIS algorithm utilises the Ross-Li BRDF model (Wanner et al., 1995).

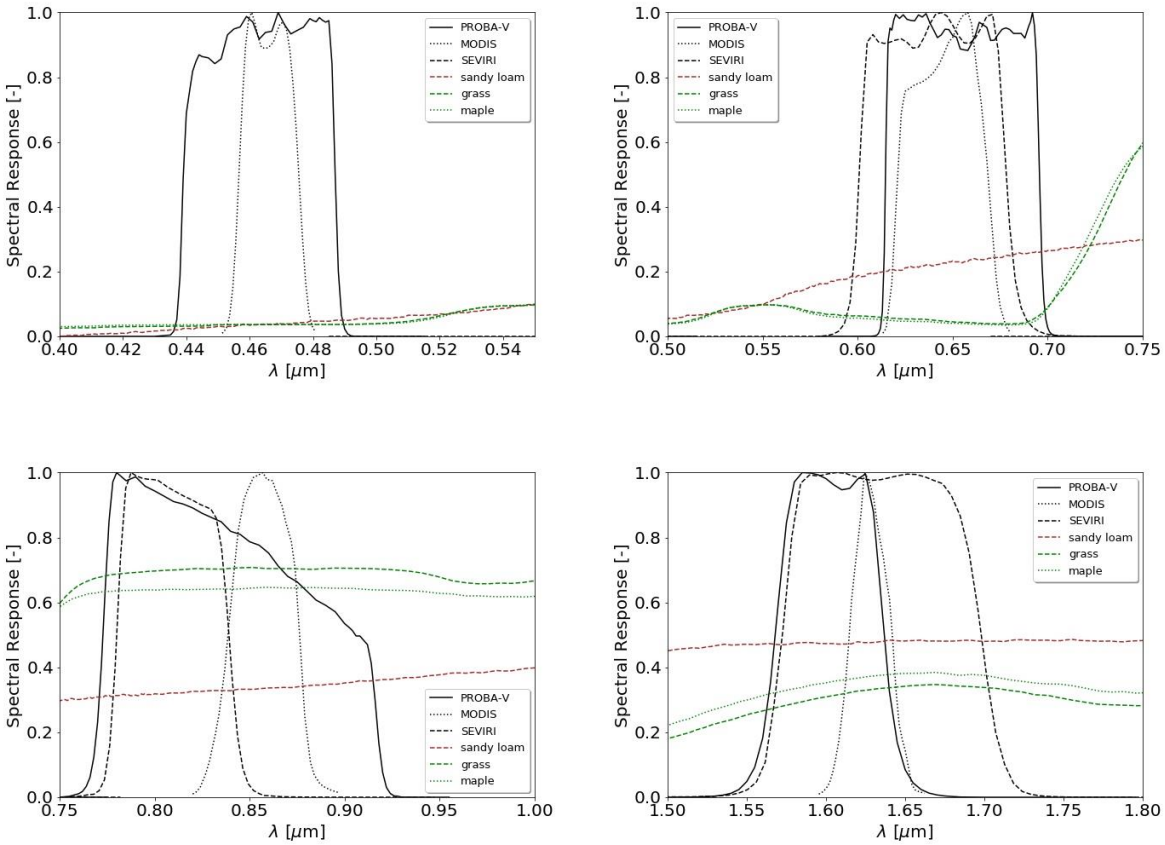

Figure 2: PROBA-V (solid lines), MODIS (dotted lines) and SEVIRI (dashed lines) Spectral Response Functions for BLUE – SWIR, clockwise from the upper left panel. Note that SEVIRI only has corresponding operational channels for the RED, NIR, and SWIR bands. Further, reflectance spectra for grass (dashed dark green line), maple leaf (dotted dark green line), and sandy loam soil (dashed brown line) are shown as reference.

CISAR and MODIS BHR values, the latter aggregated from the nominal 500 m to 1 km resolution, were collocated in time and further screened for MODIS BHR values having the overall quality flag (obtained from the MCD43A2 BRDF Quality Product) indicated as 'good', while MODIS and PROBA-V BHR inversions for which the MODIS BRDF quality was inferior were discarded from the

comparison. The BHR comparison results are provided as scatter density plots for all sites, as well as divided for the categories introduced in Section 2.1.

An additional comparison was performed using Meteosat-Spinning Enhanced Visible and Infrared Imager (SEVIRI, Schmetz et al. 2002) BHR retrievals, developed and distributed by the Land Surface Analysis Satellite Application Facility (LSA-SAF, Trigo et al., 2011). Daily BHR data were obtained from the LSA-SAF website for January 2014 – October 2015. The temporal sampling of 15 minutes enables daily BHR retrievals.

The LSA-SAF algorithm (Geiger et al., 2008) uses SMAC to correct per SEVIRI time slot the TOA-observed reflectances for atmospheric contributions, with aerosol information obtained using a static latitudinal function of Berthelot et al. (1994), yielding TOC reflectances for the three SEVIRI solar channels (centered at 0.64, 0.81, and 1.64 μm). Subsequently, the surface Bi-Directional Reflectance Distribution Function (BRDF) of Roujean et al. (1992) is applied to the daily accumulated TOC reflectances and angular integrations to obtain daily BHR values are performed. The LSA-SAF BHR performance has been evaluated against MODIS Collection 4 by Carrer et al. (2010). For spectral BHR, differences with MODIS of 15% (RED), 4% (NIR), and 11% (SWIR) were found, which were mainly attributed to differences in the BRDF inversion models of LSA-SAF and MODIS.

For the comparison, daily snow-free SEVIRI BHR and accompanying error values within 0.02^{o} of the AERONET locations were collected and Inverse Distance Weighting (IDW) was used to obtain a daily BHR value at the AERONET location. Subsequently, 16-day averages with 8 day temporal shifts were computed for dates from 1 January 2014 onwards. Figure 3 indicates the AERONET stations within the area observed by SEVIRI.

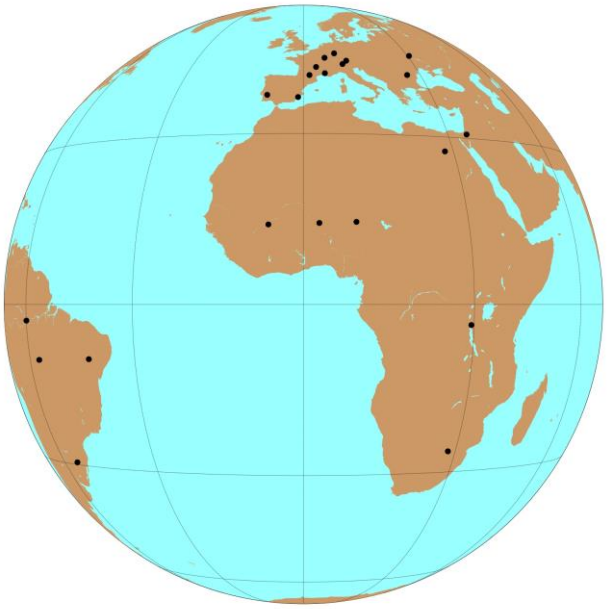

Figure 3: Locations of AERONET stations inside the SEVIRI-observed area.

For the 22 AERONET stations inside the area observed by SEVIRI, BHR time series for the CISAR, MODIS, and SEVIRI were plotted. The plots also contain the directional TOC reflectances extracted for the AERONET stations from the operational PROBA-V S10 data product.

2.3.2. DIRECTIONAL TOC REFLECTANCE VALIDATION

In order to assess the added value of the surface reflectance retrieved by CISAR to the current operational (OP) PROBA-V TOC reflectance, these values were collocated and compared with values from CISAR and MODIS, with the latter values serving as reference. In order to have comparable quantities, for the latter two datasets the retrieved RPV parameters, together with the PROBA-V viewing and illumination geometries, were used to obtain TOC reflectance approximations. Figure 4 shows the TOC reflectance intercomparison workflow.

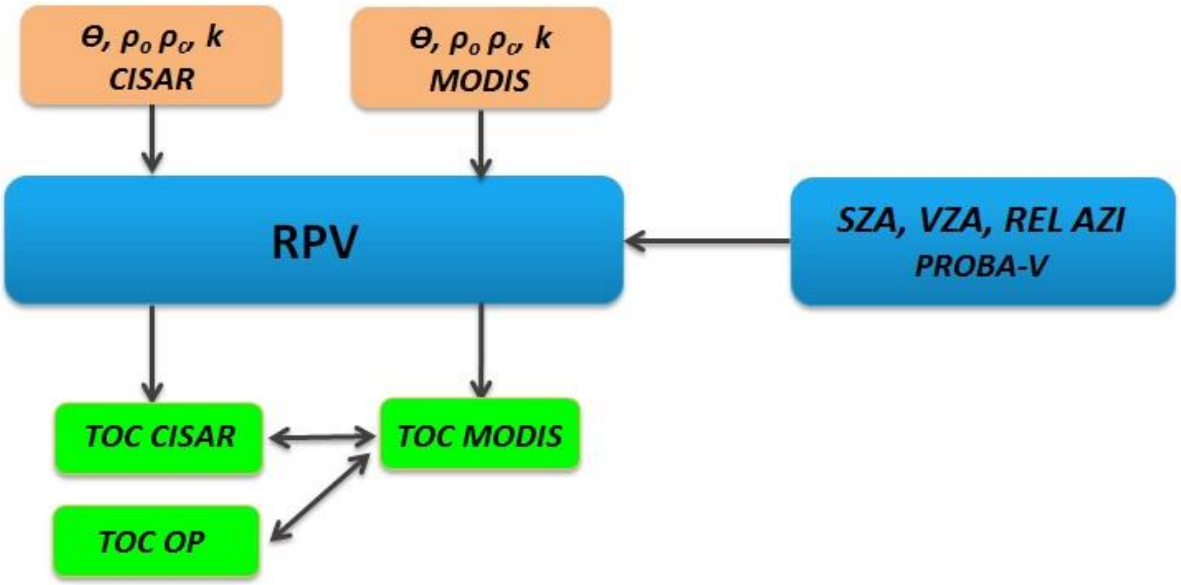

Figure 4: Flowchart of the TOC reflectance comparison between OP, CISAR, and MODIS for January 2014 – March 2015. The latter two TOC reflectance datasets were obtained using the RPV model surface parameters (ρ_c, ρ_o, Θ, and k) that were retrieved by the respective algorithms and the actual PROBA-V viewing and illumination geometries.

The TOC reflectance comparison was done as follows. For the AERONET stations shown in Error! eference source not found., the RPV parameters (ρ_c, ρ_o, k, and Θ, representing the hot spot, BRF amplitude, modified Minnaert, and Henyey – Greenstein contributions, respectively) retrieved by the CISAR and MODIS surface reflectance algorithms and the PROBA-V viewing and illumination geometries were used as input for the RPV algorithm (downloaded from http://fapar.jrc.ec.europa.eu).

PROBA-V operational TOC reflectances for January 2014 – March 2015 were obtained from intermediate Level 2B files that were temporarily stored during the 2016 PROBA-V Collection 1 reprocessing campaign. These intermediate Level 2B files comprised 5 × 5 pixel TOC reflectances extractions for all spectral bands, the viewing and illumination geometries, Status Map, as well as the AOT information over the selected AERONET stations. For the comparison between the CISAR, MODIS, and operational PROBA-V TOC reflectance datasets, only data for which the entire extracted 5 × 5 pixel areas were labelled cloud free in the Status Map were included. Additionally, in order to remove situations with non-detected clouds (e.g. thin cirrus), the operational NDVI versus TOC BLUE relation was examined, as generally undetected clouds will significantly increase the BLUE TOC reflectance. Observations for which the operational TOC NDVI was < 0.12 were considered 'cloudy' and discarded from all three datasets for all spectral channels.

CHAPTER 3 VALIDATION RESULTS

3.1. AOT VALIDATION

Figure 5 shows the AOT retrieved from CISAR compared with collocated AERONET AOT over the 50 selected stations for CISAR v2 (left panel) and v1 (right panel). The top row shows the difference between v2 and v1 when all retrievals are included, while the bottom row highlights the impact of the Quality Indicator (QI) for v2 by showing results for QI ≤ 0.2 and QI ≥ 0.8.

The top row of Figure 5 shows that an improvement is achieved for all calculated metrics. The correlation coefficient increases from 0.35 to 0.44, while accuracy, precision, and uncertainty values (hereafter referred to as *A*, *P*, and *U*) decrease from 0.14 to 0.09, 0.30 to 0.22, and 0.33 to 0.23, respectively. In addition, the scatter plots show that the prominent large overestimation for low to medium AERONET AOT (< ~0.7) has significantly decreased, although still an overestimation exists at these low AERONET AOT values. The bottom row panels indicate the difference between the CISAR v2 AOT retrievals for QI ≤ 0.2 (retrievals of low quality) vs QI ≥ 0.8 (retrievals of high quality). The number of AOT retrievals that are within the GCOS AOT retrieval accuracy requirements (indicated in Figure 5 by the dotted black lines) increases from 20.0% in v1 to 24.6% in v2, QI ≥ 0.8.

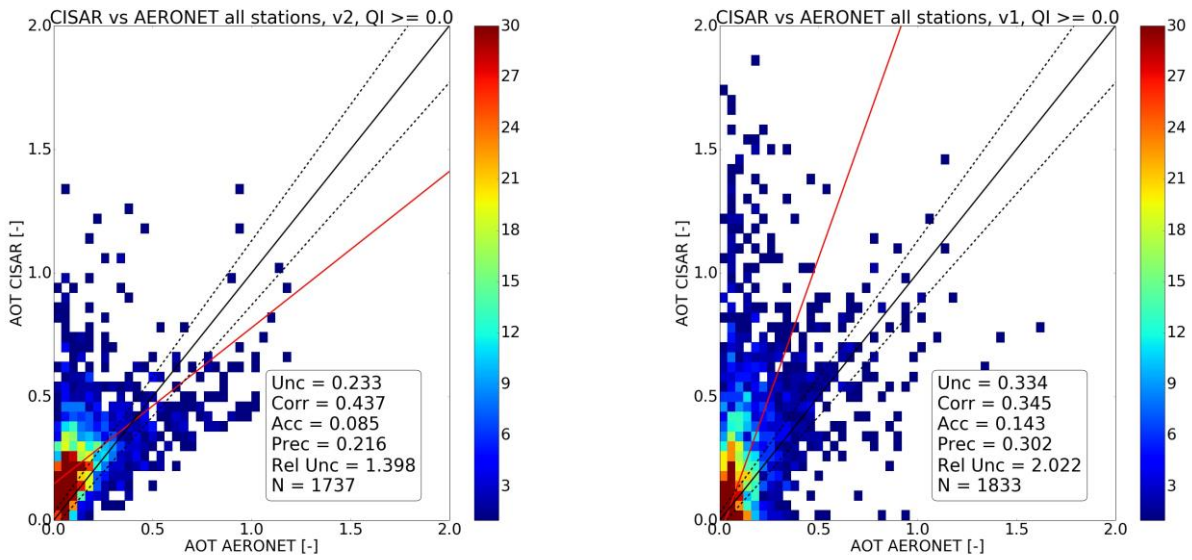

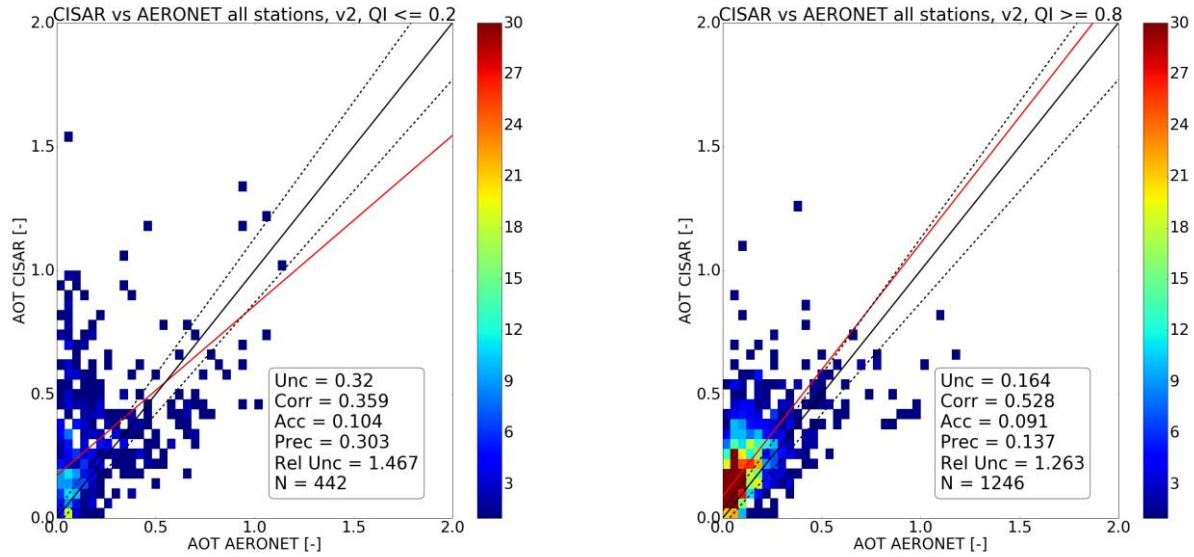

Figure 5: top row: Scatter density plots for CISAR-retrieved AOT against AERONET Level 2.0 AOT for v2 containing all retrievals (QI ≥ 0, left panel) and v1 (right panel). Bottom row: results for v2 with low (QI ≤ 0.2, left panel) and high retrieval quality (QI ≥ 0.8, right panel). The solid black line indicates the 1:1 relation, while the dotted black lines indicate the GCOS AOT target accuracy requirement of ±10%. The solid red line indicates the orthogonal least square regression and the colorbar indicates the colour coding for the bin density. All results were obtained for 2014 – 2015.

Figure 5, bottom row shows that the QI introduction significantly impacts the AOT retrieval comparison results. While *A* decreases only slightly (from 0.10 – 0.09), *U* (which is similar to *RMSE*) and *P* improve to a larger extent, with decreases from 0.32 to 0.16 and 0.30 to 0.14, respectively. The relative uncertainty shows a more dampened decrease from 1.47 to 1.26. Finally, the orthogonal linear regression is closer to the 1:1 line for retievals with QI ≥ 0.8 and has slope and intercept values of 1.021 and 0.088, respectively.

The AOT overestimation at low AERONET AOT is to be further investigated, although it might be put into a different perspective. Poulsen and Schutgens (2015) claim a low bias for AERONET Level 2.0 AOT in comparison with the ECMWF Hamburg (ECHAM) atmospheric composition model. Their suggestion was that the cloud masking over AERONET stations is probably too strict, thereby removing situations with heavy aerosol burdens from the datasets. However, their claim was not supported by evidence, so more research on this topic is required.

Figure 6 shows the AOT retrieval evaluation for the 'partial vegetation', 'full vegetation', 'bare soil', and 'mixed surface' categories for v2 and QI ≥ 0.8, i.e., including only CISAR retrievals with high quality. The panels show that *A* is comparable over AERONET stations (~0.07) with partial and full vegetation and that *A* is slightly poorer over stations with mixed surfaces and bare soils (~0.10). The values for *P* are of the same order (~0.14) over the partial and full vegetation and mixed surfaces, but are lower over bare soils (*P*=0.11). When considering the uncertainty, we see that the absolute values are 0.15 – 0.17 over the four categories, but that values for relative uncertainty vary substantially more (0.90 – 1.65), with the lowest (most favourable) value over partially vegetated surfaces. The orthogonal regressions are closest to 1:1 for partial vegetation and bare soils, while considerably higher slope values were found over full vegetation and mixed surfaces.

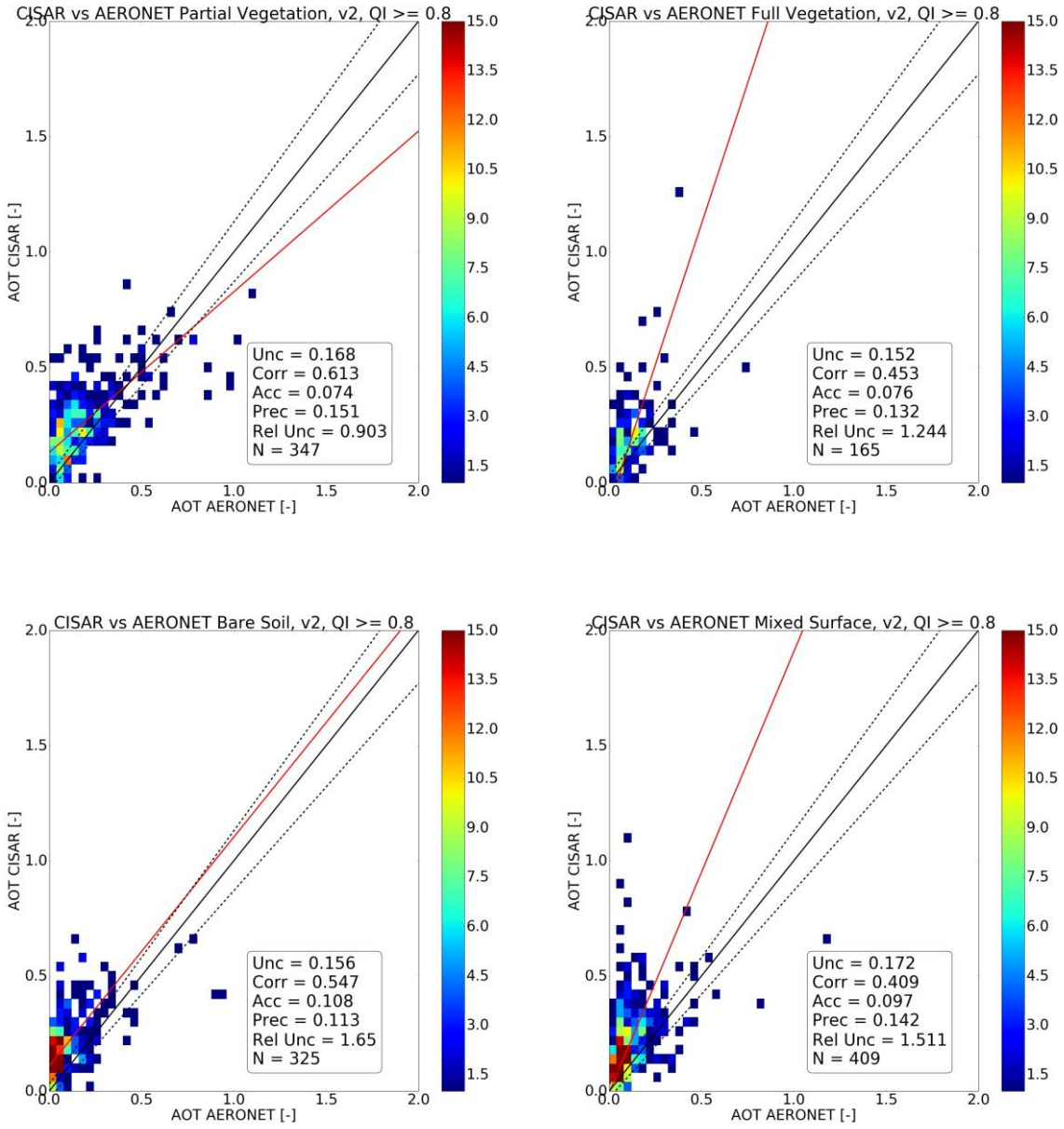

Figure 6: CISAR AOT retrievals versus AERONET AOT for v2, QI ≥ 0.8 over stations with partial vegetation (upper left), full vegetation (upper right), bare soil (lower left), and mixed surface (lower right).

3.2. SURFACE REFLECTANCE VALIDATION

3.2.1. BI-HEMISPHERICAL REFLECTANCE

→ BHR scatter plots

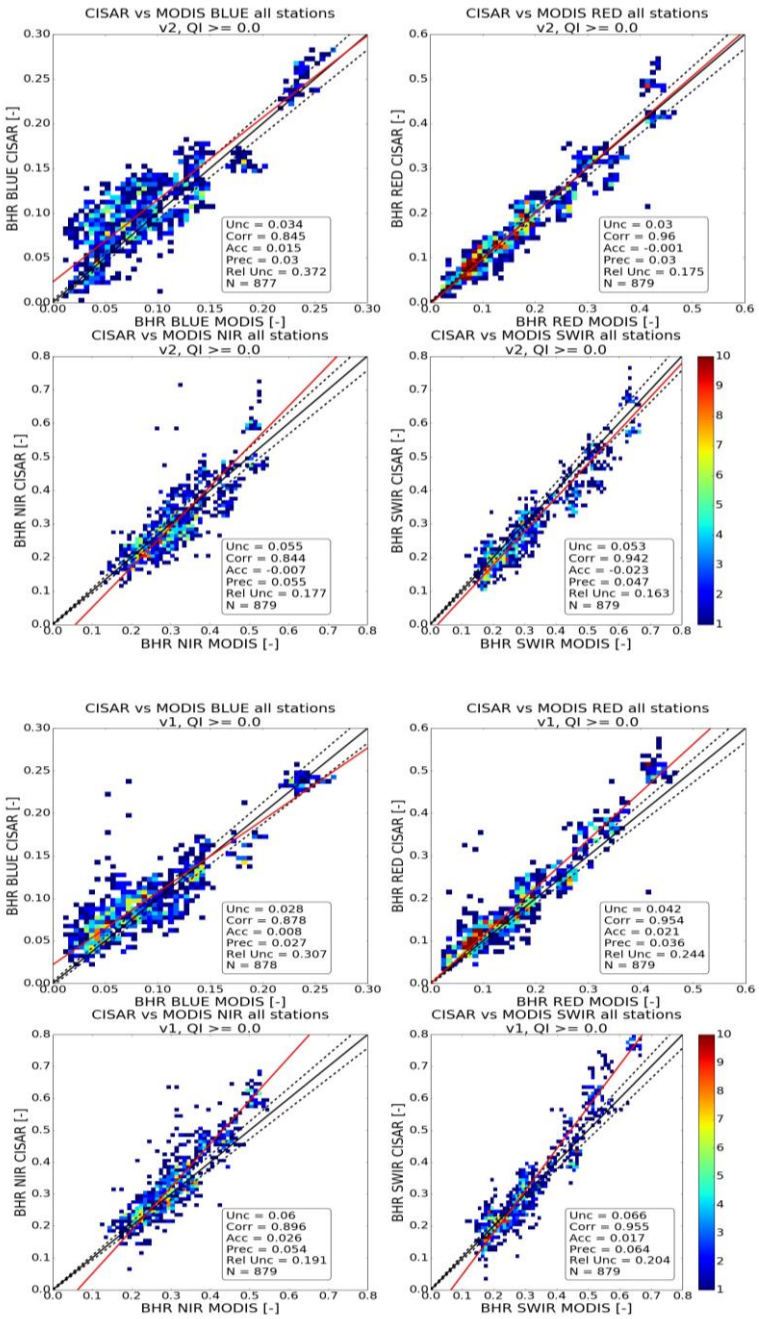

Figure 7: Scatter density plots for CISAR versus MODIS BHR over all AERONET stations for v2, QI ≥ 0 (upper 4 panels) and v1 (lower 4 panels). For each panel group, BLUE is presented upper left, RED upper right, NIR lower left, and SWIR lower right. Solid black lines indicate the 1:1 relation, dotted black lines denote the GCOS SR accuracy target of ±5%. The solid red line shows the orthogonal linear least square regression and the colour bar indicates the colour coding for the bin density. All results were obtained for 2014 – 2015.

Figure 7 shows the scatter density plots of the CISAR BHR compared to MODIS BHR. As for the AOT validation, we first show the difference between v2 and v1 over all AERONET stations and with no QI filtering for v2. For the BLUE channel, results have slightly decreased for v2, mainly for accuracy and relative uncertainty, for which values have become 0.015 and 0.372, respectively. However, the orthogonal regression indicates that the retrievals are approaching the 1:1 line compared to v1; the slope value increases from 0.849 in v1 to 0.918 in v2.

For the RED, NIR, and SWIR channels, a clear improvement for v2 is visible. For the RED channel, an almost perfect accuracy of -0.001 is achieved in v2 and the precision and relative uncertainty decrease from 0.036 to 0.03 and 0.24 to 0.18, respectively. In addition, the regression slope value significantly improves from 1.124 to 1.02. The NIR channel shows a large accuracy improvement from 0.026 to -0.007 and a regression slope value decrease from 1.357 to 1.202, whereas *P* and *U* only express small changes. For the SWIR channel, a remarkable change of sign for *A* is seen (0.017 to -0.023). The small decrease in performance in *A* is opposed by slight improvements in *P* and *U*, with values decreasing from 0.064 to 0.047 and 0.066 to 0.053, respectively. A significant improvement, however, is observed for the regression slope and intercept values, which change from 1.315 to 1.003 and -0.085 to -0.024, respectively.

Figure 8 presents the comparison between low- and high-quality retrievals for BHR versus MODIS. For the BLUE channels, the difference between low and high quality retrievals results in a slight decrease in performance, which mainly holds for the relative uncertainty that increases from 0.36 to 0.41. For the RED channel, the performance metrics remain virtually unaffected, but the regression line gets closer to the 1:1 line and improves from $BHR_{RED,CISAR} = 1.090 * BHR_{RED,MODIS} - 0.015$ to $BHR_{CISAR} = 0.982 * BHR_{MODIS} + 0.001$. A similar pattern is seen for the NIR and SWIR channels, here the orthogonal regressions improve from $BHR_{NIR,CISAR} = 1.350 * BHR_{NIR,MODIS} - 0.114$ to $BHR_{NIR,CISAR} = 1.143 * BHR_{NIR,MODIS} - 0.052$ and $BHR_{SWIR,CISAR} = 1.068 * BHR_{SWIR,MODIS} - 0.050$ to $BHR_{NIR,CISAR} = 0.956 * BHR_{NIR,MODIS} - 0.009$. Table 1 presents the regression slope and intercept values for the v2 low- and high-quality retrievals.

Table 1: Orthogonal regression slope and intercept values of CISAR v2 BHR retrievals on MODIS BHR for retievals with QI ≤ 0.2 and QI ≥ 0.8.

	CISAR v2 QI ≤ 0.2		**CISAR v2 QI ≥ 0.8**	
	slope	**intercept**	**slope**	**intercept**
BLUE	0.958	0.018	0.923	0.024
RED	1.090	-0.015	0.982	0.001
NIR	1.350	-0.114	1.143	-0.052
SWIR	1.068	-0.050	0.956	-0.009

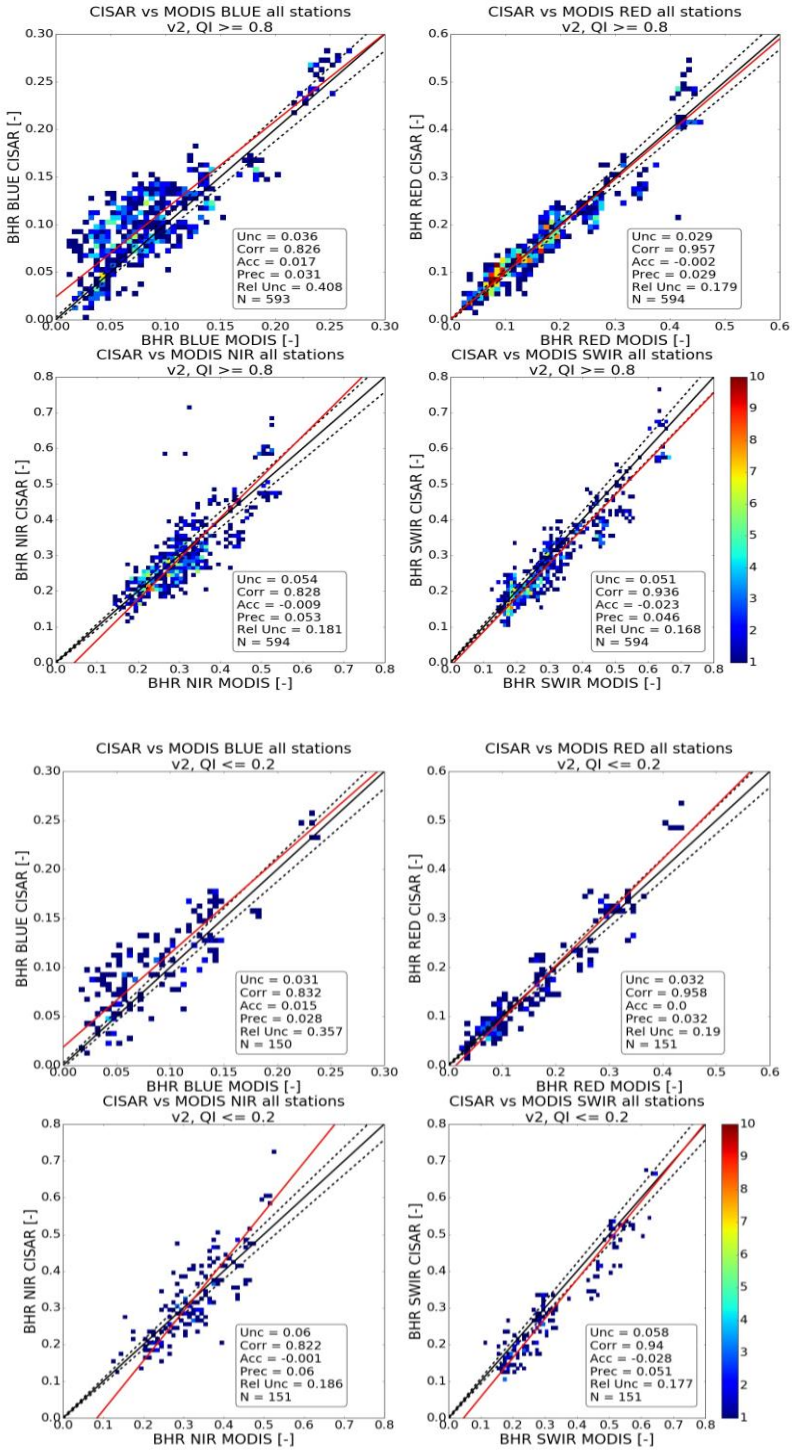

Figure 8: CISAR BHR versus MODIS BHR retrievals for QI ≥ 0.8 (upper 4 panels) and QI ≤ 0.2 (lower 4 panels).

Figure 9 shows scatter plots of CISAR BHR retrievals with QI ≥ 0.8 compared with LSA-SAF BHR retrievals based on Meteosat-SEVIRI observations. Note that the comparison with SEVIRI retrievals could only be performed for the RED – SWIR spectral channels, as SEVIRI does not observe in the BLUE spectral range (except for the non-operational High Resolution Visible channel, 0.4 – 1.1 µm).

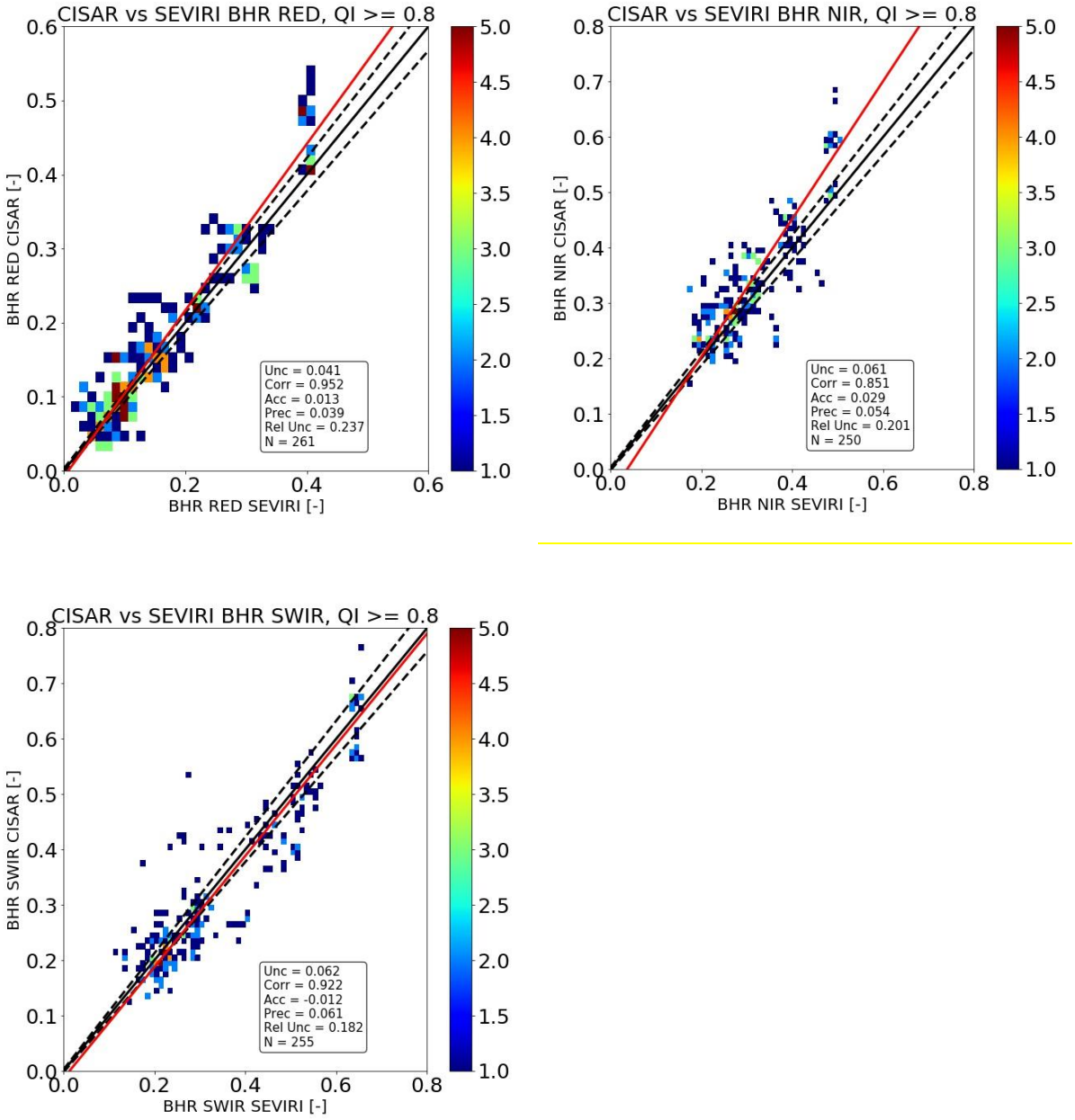

Figure 9: Scatter density plots for CISAR BHR retrievals versus LSA-SAF Meteosat-SEVIRI BHR for high-quality retrievals (QI ≥ 0.8). Note the different density colour range compared to the previous Figures.

From <cross ref9> it follows that, as for the comparison with MODIS BHR retrievals, the results for RED – SWIR compared to SEVIRI are promising. Accuracy ranges from -0.01 – 0.03, precision from 0.04 – 0.06, and relative uncertainty is 0.18 – 0.24. This proves that, despite the various observational (spectral, spatial, and temporal resolution) and algorithmic differences (BRDF characterisation and aerosol optical thickness and atmospheric correction), CISAR is able to accurately retrieve BHR.

In order to get a further indication on to which extent CISAR is able to retrieve consistent BHR time series in relation to its MODIS and SEVIRI counterparts over various land surfaces Figure 10 – Figure 13 show time series over selected AERONET stations within the MSG disk. To have as complete CISAR BHR time series as possible, no BHR retrieval quality filtering was applied. Further, directional TOC reflectances were extracted from PROBA-V S10 product data to assess whether the temporal signal of the retrieved BHR is smoother.

The time series over Banizoumbou (Figure 10) show that the CISAR temporal signature is consistent with that of MODIS, SEVIRI, and the operational S10 directional TOC reflectance. Further, the CISAR BHR retrievals are considerably smoother than the TOC reflectances from the S10 product. In the BLUE channel, CISAR exhibits a small underestimation relative to MODIS during 2014, which changes into an overestimation during 2015. In the RED channel, CISAR BHR changes in a similar way as MODIS and SEVIRI, with CISAR and MODIS having similar absolute values. The lower SEVIRI RED BHR might be partly due to the spectral channel being shifted to lower wavelengths. This results in a slightly lower reflectance when vegetation is absent, which occurs in the Sahel zone outside of the monsoon season. However, various factors between the different algorithms play a role in deriving the respective BHR datasets and detailed research would be required to attribute the observed differences to the various algorithm steps (atmospheric correction, BRDF model inversion, spectral response, temporal sampling and weighing, etc.).

Also for the NIR and SWIR channel, the CISAR BHR retrievals are closer to MODIS than to SEVIRI, although during 2015 the CISAR BHR values are lower than those of MODIS. Nevertheless, the temporal evolution of CISAR and MODIS is similar.

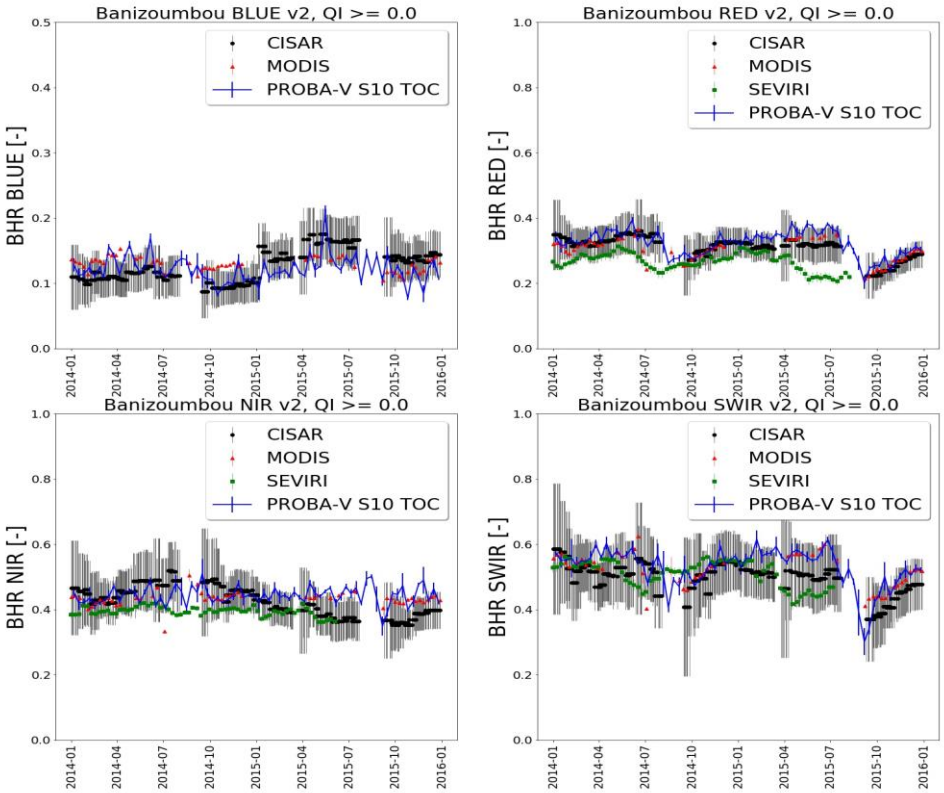

Figure 10: BHR time series (2014 – 2015, BLUE – SWIR clockwise from the upper left) over Banizoumbou (Niger) for CISAR (black circles), MODIS (red triangles), SEVIRI (green squares), and directional TOC reflectance (blue solid lines) extracted from the PROBA-V S10 data product. Note the different y axis range for the BLUE channel.

Figure 11 shows the time series over Carpentras (France). In general, the CISAR and MODIS BHR retrievals show a consistent temporal signature and both have a lower amplitude than SEVIRI. For the BLUE channel, CISAR has comparable values as MODIS, which changes into a considerable overestimation (~0.05) during 2015. This pattern was seen over almost all AERONET stations within the SEVIRI observation area (except for Sede Boker) and examination of the respective AOT time series revealed no abrupt changes.

In the RED channel, CISAR and MODIS have an almost perfect agreement throughout the entire period, with both a considerably lower amplitude than the SEVIRI BHR. For NIR, CISAR and MODIS agree well in terms of absolute values and temporal evolution, with both a similar decrease (from 0.35 down to ~0.25) during autumn. Further, both CISAR and MODIS have BHR values about 0.10 higher than SEVIRI and their peak values are about 1 month later. During the first half of 2015, CISAR is in closer agreement with SEVIRI, while MODIS shows a steeper increase during spring and higher absolute values throughout summer. For SWIR, CISAR's temporal evolution is again similar to that of MODIS, although absolute values are about 0.05 lower than MODIS during 2015.

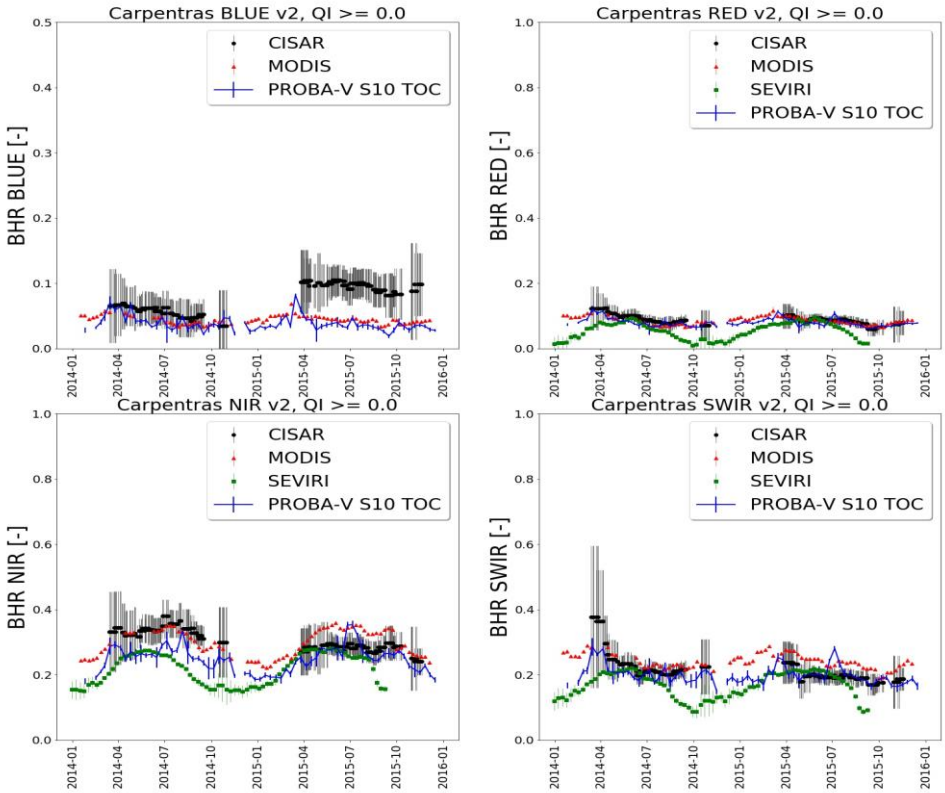

Figure 11: Same as Figure 10*, but for Carpentras (France). Note the different y axis range for the BLUE channel.*

The time series for El Farafra (Egyptian desert, Figure 12) show similar patterns for the BLUE channel; CISAR agrees very well with MODIS during 2014, while its values are 0.04 – 0.06 higher during 2015. For the RED – SWIR channel, CISAR has higher values than MODIS and SEVIRI, which gradually decrease and finally results in close agreement with MODIS and SEVIRI during 2015 for the RED channel and lower values for the NIR and SWIR channels. Finally, it is noted that BHR retrievals for all methods yield a smoother signal than the directional S10 TOC reflectances.

The time series for Murcia (Spain) are presented in Figure 13. As for the other three time series that are shown in this report, the BLUE CISAR BHR agrees very well during 2014, except for CISAR being higher during May – June 2014. However, during 2015 the CISAR BHR BLUE again is much higher than MODIS, with values hovering around 0.12 compared to ~0.07 for MODIS. In the RED channel, CISAR and MODIS values agree closely and both exhibit a smaller BHR amplitude compared to SEVIRI. The close agreement in absolute BHR values and its temporal evolution is also shown for the NIR and SWIR channels during 2014. However, note the lower CISAR values compared to MODIS in the NIR and the apparent NIR BHR phase shift of CISAR and MODIS with SEVIRI NIR BHR.

Finally, during May – August 2015 for RED – SWIR the directional S10 TOC reflectances are considerably higher than the corresponding CISAR BHR values.

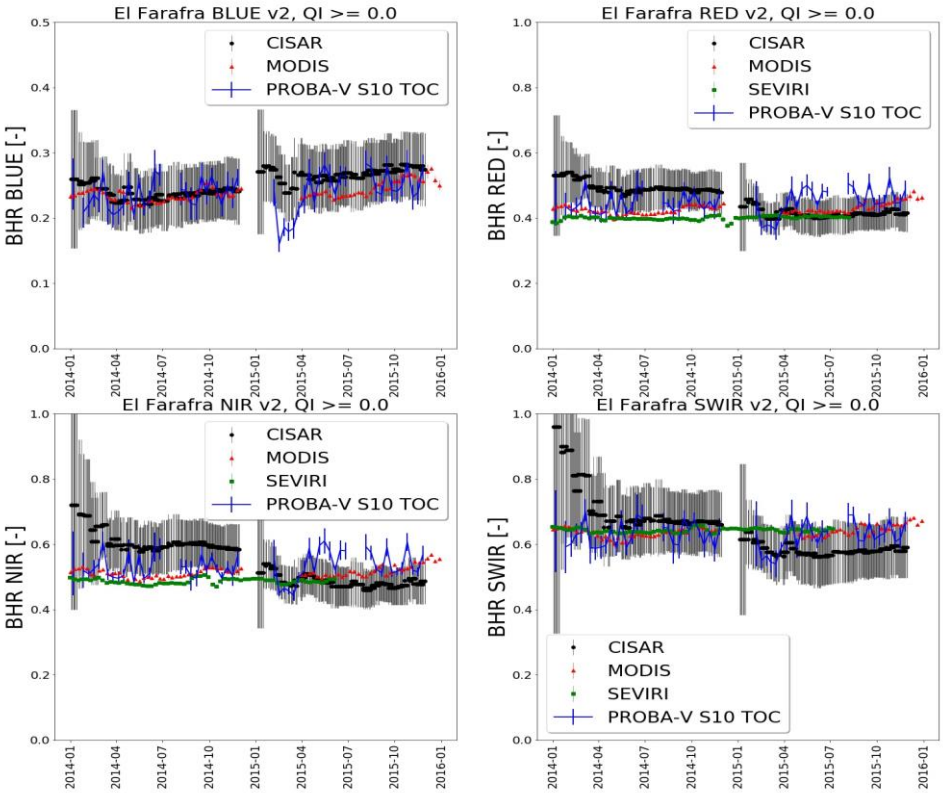

Figure 12: Same as Figure 10*, but for El Farafra (Egypt). Note the different y axis range for the BLUE channel.*

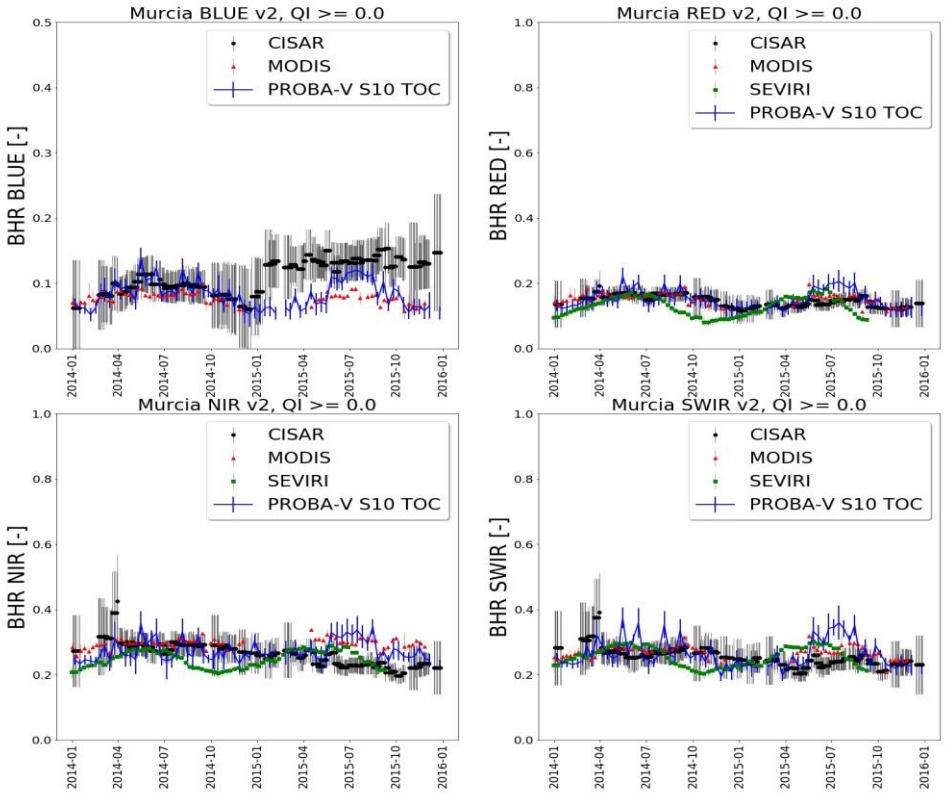

Figure 13: Same as Figure 10*, but for Murcia (Spain). Note the different y axis range for the BLUE channel.*

→ **BHR APU plots**

In order to get an indication of the BHR accuracy, precision, and uncertainty as function of the MODIS reference BHR, so-called APU plots (Claverie et al., 2015) were made. As for the AOT and BHR scatter plots, the plots are shown for CISAR v1 and v2, all retrievals included for the latter, as well as for the low- (QI ≤ 0.2) and high-quality (QI ≥ 0.8) v2 retrievals. **Error! Reference source not ound.**Figure 14 shows the APU plots for v1 and v2, all retrievals. The solid black line denotes the GCOS SR target accuracy. The plots show that for the BLUE channel, in the low BHR range (< ~0.30) the v2 *A*, *P*, and *U* show slightly higher values (i.e., less favourable) compared to v1. This is in accordance with the scatter plot results of Figure 7. The slight decrease in performance statistics for the BLUE channel and overestimation relative to MDOIS BHR might not necessarily hint for a decrease in CISAR v2 performance, as the MODIS Collection 5 data products were significantly impacted by calibration degradation due to Solar Diffuser (SD) issues on the MODIS Terra platform. This degradation was largest in the MODIS BLUE band (center wavelength 0.469 µm) and resulted in long-term negative trends in among others aerosol optical thickness and surface reflectance (Lyapustin et al., 2014). The calibration issues were corrected for in the Collection 6 dataset.

For the RED and NIR channels, the APU plots show a significant improvement for BHR <~0.4, while for the SWIR channel the differences between v2 an v1 are negligible.

Figure 14 also shows that the accuracy, precision, and uncertainty values are not fulfilling the GCOS 5% surface reflectance target accuracy yet. Nevertheless, these results are promising, given the fact that this comparison was performed against MODIS BHR and the differences in the PROBA-V and MODIS spectral responses, the sensors' spatial resolution (500 m versus 1 km), as well as different atmospheric correction and BRDF normalisation algorithms certainly play a role. Moreover, although MODIS surface albedo retrievals were extensively evaluated with *in situ* measurements and agreement is very good for homogeneous surfaces, a larger difference is seen for heterogeneous surfaces (see e.g. Cescatti et al., 2012 and Román et al. 2013). Overall, the MODIS surface albedos are within ±10% for SZA < 70^{o}.

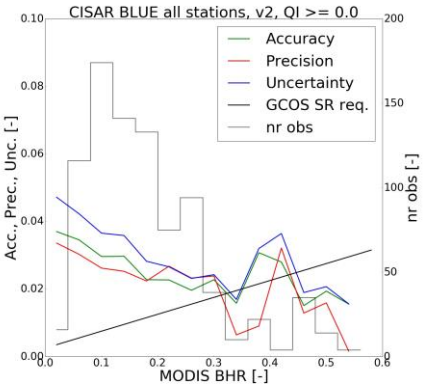
CISAR BLUE all stations, v2, QI >= 0.0
Accuracy
Precision
Uncertainty
GCOS SR req.
nr obs
Acc., Prec., Unc. [-]
nr obs [-]
MODIS BHR [-]

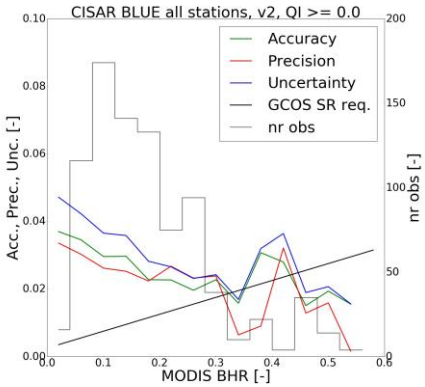
CISAR BLUE all stations, v2, QI >= 0.0
Accuracy
Precision
Uncertainty
GCOS SR req.
nr obs
Acc., Prec., Unc. [-]
nr obs [-]
MODIS BHR [-]

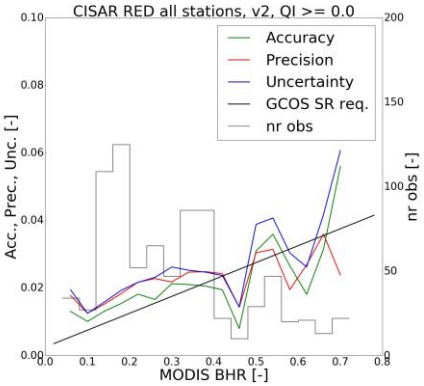
CISAR RED all stations, v2, QI >= 0.0
Accuracy
Precision
Uncertainty
GCOS SR req.
nr obs
Acc., Prec., Unc. [-]
nr obs [-]
MODIS BHR [-]

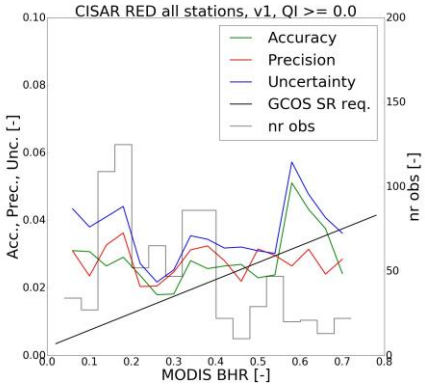
CISAR RED all stations, v1, QI >= 0.0
Accuracy
Precision
Uncertainty
GCOS SR req.
nr obs
Acc., Prec., Unc. [-]
nr obs [-]
MODIS BHR [-]

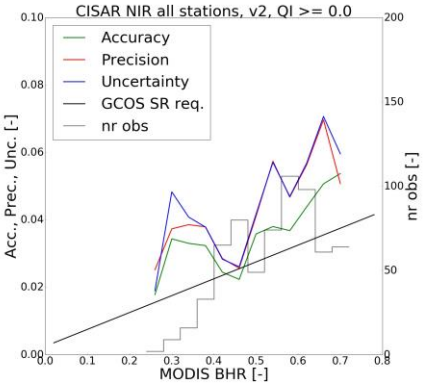
CISAR NIR all stations, v2, QI >= 0.0
Accuracy
Precision
Uncertainty
GCOS SR req.
nr obs
Acc., Prec., Unc. [-]
nr obs [-]
MODIS BHR [-]

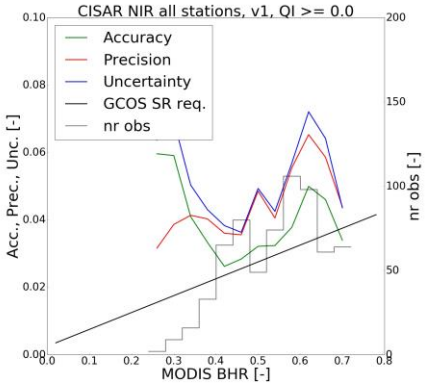
CISAR NIR all stations, v1, QI >= 0.0
Accuracy
Precision
Uncertainty
GCOS SR req.
nr obs
Acc., Prec., Unc. [-]
nr obs [-]
MODIS BHR [-]

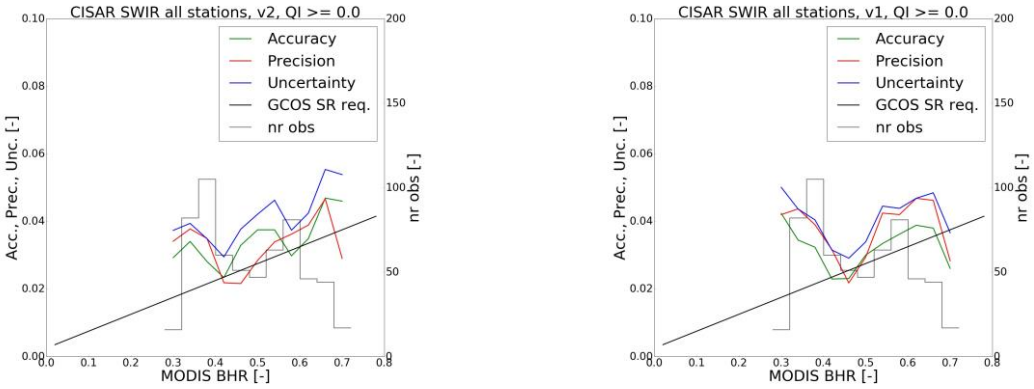

Figure 14: APU plots for CISAR BHR against MODIS BHR for the BLUE (top row), RED (2nd row), NIR (3rd row), and SWIR (bottom row), as function of MODIS BHR for CISAR v2 (left column panels) and CISAR v1 (right column panels), all retrievals included.

3.2.2. TOP-OF-CANOPY REFLECTANCE

Figure 15 shows per PROBA-V spectral channel scatter plots of TOC reflectances for CISAR v2, MODIS (both derived from the respective RPV parameters), and the current operational (OP) TOC reflectances. See Figure 4 for the workflow. For the BLUE channel, the calculated CISAR TOC reflectances show a better agreement with MODIS, with an accuracy of virtually zero and precision and relative uncertainty decreasing from 0.035 to 0.018 and 0.52 to 0.22, respectively, thereby indicating an improvement over the OP TOC reflectances.

Also for the RED channel, all performance metrics for CISAR indicate better agreement with MODIS than for OP, although CISAR tends to overestimate the TOC reflectance relative to MODIS beyond ~0.15. For the NIR channel, the accuracy shows no improvement, however, the precision and uncertainty metrics do indicate better agreement with the calculated reference MODIS TOC reflectances. Finally, for the SWIR channel the CISAR TOC reflectances show a marginal improvement for all performance metrics. Because aerosols have only a very small contribution in this spectral range, a small difference between the CISAR and SMAC atmospheric correction algorithms was expected.

The observed differences between the TOC reflectances obtained from the CISAR- and MODIS-retrieved RPV parameters can be linked to a combination of the spectral response differences and the derived RPV parameters. For example, examination of the retrieved parameters (not shown) indicates a considerable difference in the hot-spot parameter $\rho_{c,}$, with the MODIS ρ_c parameter mainly having a larger dynamic range (typically 0.1 – 0.9 vs 0.4 – 0.7). Because the MODIS RPV parameters were retrieved from both Terra and Aqua observations, it is expect that observing the surface at multiple times during a day causes this difference in dynamic range.

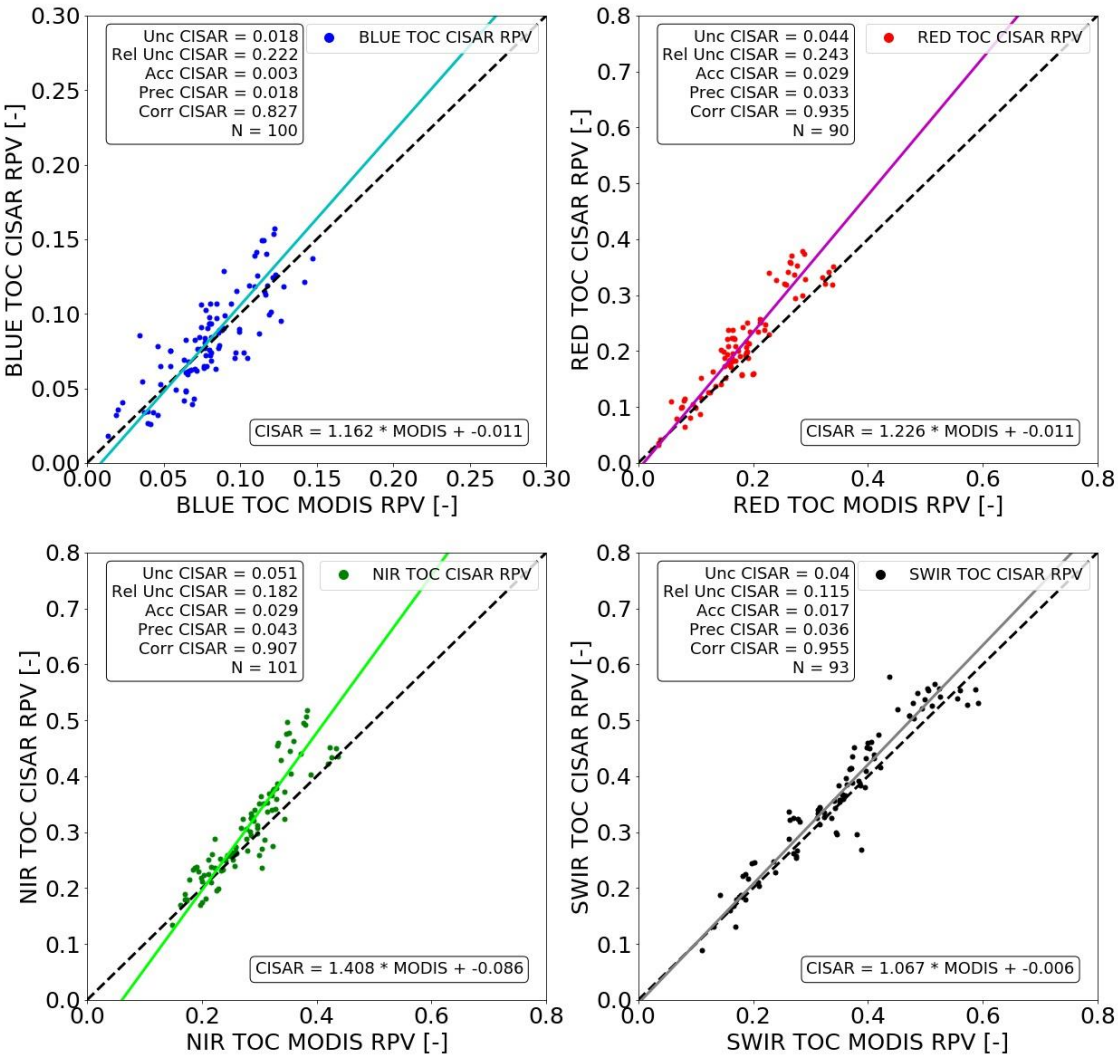
Unc CISAR = 0.018
Rel Unc CISAR = 0.222
Acc CISAR = 0.003
Prec CISAR = 0.018
Corr CISAR = 0.827
N = 100
BLUE TOC CISAR RPV
CISAR = 1.162 * MODIS + -0.011
BLUE TOC CISAR RPV [-]
BLUE TOC MODIS RPV [-]
Unc CISAR = 0.044
Rel Unc CISAR = 0.243
Acc CISAR = 0.029
Prec CISAR = 0.033
Corr CISAR = 0.935
N = 90
RED TOC CISAR RPV
CISAR = 1.226 * MODIS + -0.011
RED TOC CISAR RPV [-]
RED TOC MODIS RPV [-]
Unc CISAR = 0.051
Rel Unc CISAR = 0.182
Acc CISAR = 0.029
Prec CISAR = 0.043
Corr CISAR = 0.907
N = 101
NIR TOC CISAR RPV
CISAR = 1.408 * MODIS + -0.086
NIR TOC CISAR RPV [-]
NIR TOC MODIS RPV [-]
Unc CISAR = 0.04
Rel Unc CISAR = 0.115
Acc CISAR = 0.017
Prec CISAR = 0.036
Corr CISAR = 0.955
N = 93
SWIR TOC CISAR RPV
CISAR = 1.067 * MODIS + -0.006
SWIR TOC CISAR RPV [-]
SWIR TOC MODIS RPV [-]

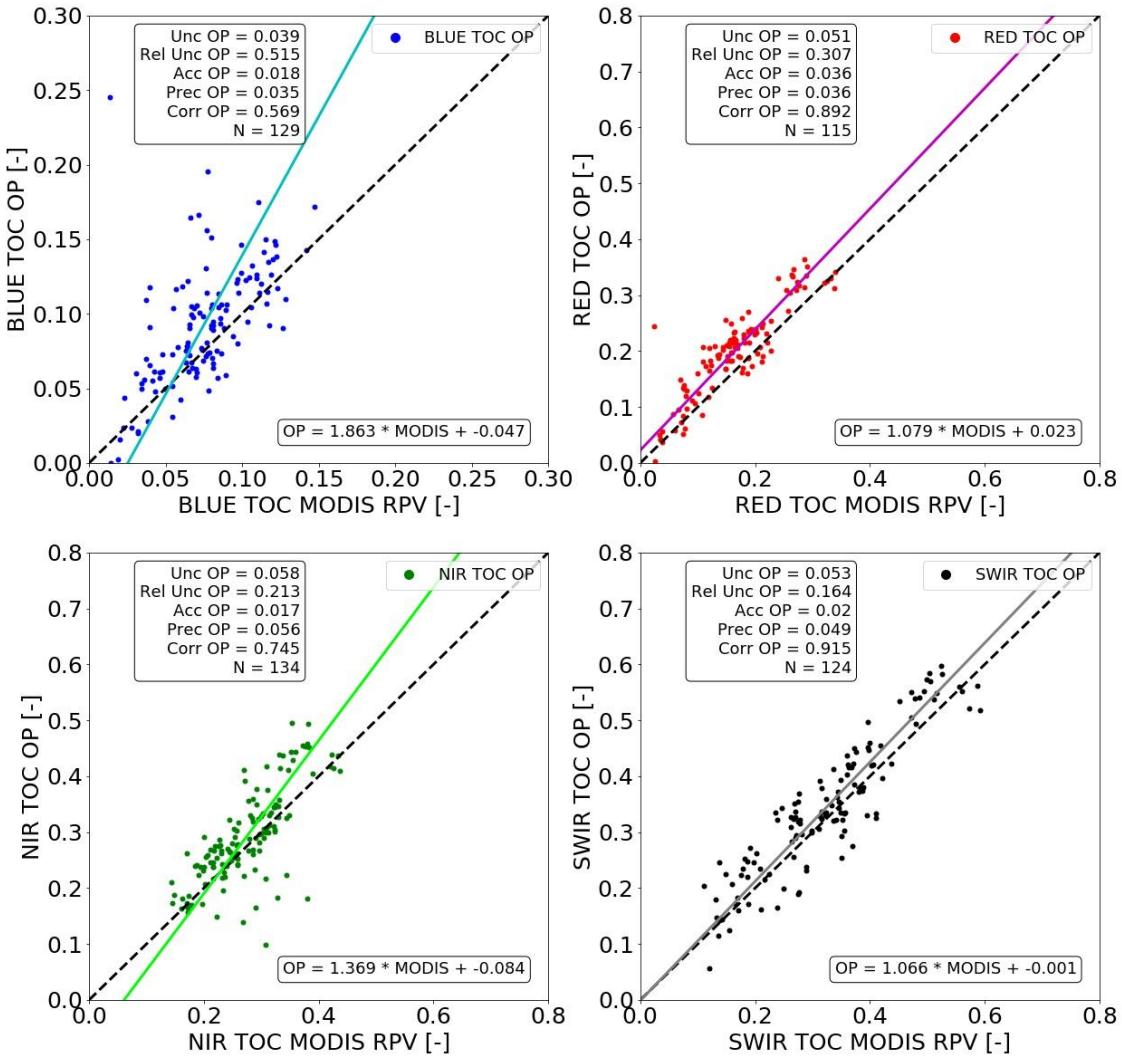

Figure 15: CISAR v2 versus MODIS TOC reflectances, both obtained using the retrieved RPV parameters from the respective algorithms (QI ≥ 0.8, upper 4 panels, BLUE to SWIR from the upper-left in a clockwise rotation) and current operational TOC reflectances (denoted OP) versus MODIS TOC reflectances (lower 4 panels). The dashed black line indicates the 1:1 relation, while solid lines denote the least square regressions. Note the different axis ranges for the BLUE and RED channels.

CHAPTER 4 SUMMARY

This report presented the validation of AOT and Surface Reflectance (in terms of Bi-Hemispherical Reflectance) from the CISAR algorithm, version 2, with AERONET AOT observations and MODIS and Metosat-SEVIRI BHR reflectances. The validation revealed the following:

- The large AOT overestimation that was seen for CISAR v1 is considerably reduced for v2. When only the high-quality retrievals of v2 are used (QI ≥ 0.8), the accuracy becomes 0.08 (was 0.13 for v1), while the relative uncertainty decreases sharply to 1.17 (was 1.81 for v1). Accuracy is slightly better over partial and full vegetation, while precision values are lowest (least scatter) over bare soils.
- For BHR, accuracy and precision values did not improve for the BLUE channel with respect to v1, which was expected from the improved AOT retrieval performance statistics. However, the BLUE regression slope and intercept values improved for v2 and become 0.92 and 0.02 for the v2 high-quality retrievals. For the RED – SWIR channels, generally an improvement for all performance metrics from v1 to v2 is observed. Regression slope and intercept values approach 1 and 0, respectively, further demonstrating increased agreement with MODIS BHR compared to the v1 validation results.
- Examination of the BHR Accuracy, Precision, and Uncertainty as function of the MODIS BHR indicates a slight decrease in performance for the BLUE BHR, especially for MODIS BHR < ~0.30. For the other PROBA-V channels, a clear performance improvement is seen, in accordance with the results of the scatter plots. The GCOS 5% SR accuracy target is not yet met, but is certainly further approached from v1 to v2.
- Comparison with 16-day averages of daily LSA-SAF SEVIRI BHR retrievals shows good agreement for the RED – SWIR channels, with accuracy and relative uncertainty ranging from -0.01 – 0.03 and 0.18 – 0.24, respectively.
- BHR time series for CISAR, MODIS, SEVIRI, and the PROBA-V S10 directional TOC reflectances reveal that CISAR BHR has generally a consistent temporal evolution and has a smoother temporal signature than the S10 TOC reflectance. Further, it was shown that CISAR and MODIS have a lower BHR amplitude than SEVIRI, but that for most situations the temporal evolution of the three datasets is consistent. However, it was also revealed that CISAR overestimates relative to MODIS in the BLUE channel during 2015, a pattern that was seen at almost all stations within the SEVIRI-observed area for which the time series plots were made. Examination of the AOT time series for each of these stations did not indicate a sudden change in the retrieved AOT between 2014 and 2015. It is thus unclear what causes this sudden BHR increase for the BLUE channel.
- Comparison of CISAR and OP TOC reflectances with MODIS TOC reflectances revealed that for all channels the precision and uncertainty for CISAR significantly decrease, indicating an added value of the CISAR atmospheric correction to the current operational SMAC algorithm. Also the accuracy improves, except for the NIR channel.

LITERATURE

Ackerman, S. A., R.E. Holz, R. Frey, E.W. Eloranta, B.C. Maddux, and M. McGill, Cloud detection with MODIS. Part II: validation. *J. Atmos. Ocean. Technol.*, 25, 1073-1086, 2008.

Berthelot, B. and G. Dedieu, Correction of atmospheric effects for VEGETATION data. *Physical Measurements and Signatures in remote sensing*, p.19 – 25, 1997.

Carrer, D., J.L Roujean, and C. Meurey, Comparing operational MSG/SEVIRI land surface albedo products from Land SAF with ground measurements and MODIS. *IEEE Transactions on Geoscience and Remote Sensing*, *48*(4), 1714-1728, 2010.

Cescatti, A., B. Marcolla, S.K.S. Vannan, J.Y. Pan, M.O. Román, X. Yang, Philippe Ciais, Robert B. Cook, Beverly E. Law, G. Matteucci, M. Migliavacca, E. Moors, A.D. Richardson, G. Seufert, and C.B. Schaaf, Intercomparison of MODIS albedo retrievals and in situ measurements across the global FLUXNET network. *Remote Sens. Environ.*, 121, 323-334, 2012.

Claverie, M., E. F. Vermote, B. Franch, and J.G. Masek, Evaluation of the Landsat-5 TM and Landsat-7 ETM+ surface reflectance products. *Remote Sens. Environ.*, 169, 390-403, 2015.

Frey, R. A., S. A. Ackerman, Y. Liu, K.I. Strabala, H. Zhang, J.R. Key, and X. Wang, Cloud detection with MODIS. Part I: Improvements in the MODIS cloud mask for Collection 5. *J. Atmos. Ocean. Technol.,* 25, 1057 – 1072, 2008.

Geiger, B., D. Carrer, L. Franchisteguy, LJ. L. Roujean, and C. Meurey, Land surface albedo derived on a daily basis from Meteosat Second Generation observations. *IEEE Transact. Geosci. Remote*, 46(11), 3841-3856, 2008.

Govaerts, Y., and M. Luffarelli, 2017, Joint retrieval of surface reflectance and aerosol properties with continuous variations of the state variables in the solution space: Part 1: theoretical concept, *Atmos. Meas. Tech. Discuss.*, https://doi.org/10.5194/amt-2017-29, 2007.

Lucht, W., C.B. Schaaf, and A.H. Strahler, An algorithm for the retrieval of albedo from space using semiempirical BRDF models. *IEEE Transact. Geosci. Remote*, 38(2), 977 – 998, 2000.

Lyapustin, A., Y. Wang, X. Xiong, G. Meister, S. Platnick, R. Levy, R., B. Franz, S. Korkin, T. Hilker, J. Tucker, F. Hall, P. Sellers, A. Wu, and A. Angal, Scientific impact of MODIS C5 calibration degradation and C6+ improvements, *Atm. Meas. Tech.*, 7, 4353 – 4365, doi:10.5194/amt-7-4353-2014, 2014.

Maisongrande, P., B. Duchemin, B.D. Berthelot, C. Dubegny, G. Dedieu, and M. Leroy, New composite products derived from the SPOT/VEGETATION mission. In *Physical measurements & signatures in remote sensing. International symposium* (pp. 239-248), 2001.

Poulsen, C. and N. Schutgens, Validation of Metop PMAp A products using AATSR Aerosol CCI data and the ECHAM Model Data, *EUMETSAT ITT 13/207655*, available at http://eumetsat.int, 66 pp, 2015.

Rahman, H., B. Pinty, and M. M. Verstraete, Coupled surface-atmosphere reflectance

(CSAR) model. 2. Semiempirical surface model usable with NOAA Advanced Very High Resolution Radiometer Data. *J. Geophys. Res.*, 98(D11), 20, 791–20, 801, 1993.

Román,M. O., C. K. Gatebe, Y. Shuai, Z. Wang, F. Gao, J. Masek, T. He, S. Liang, C. B. Schaaf, Use of In Situ and Airborne Multiangle Data to Assess MODIS- and Landsat-Based Estimates of Directional Reflectance and Albedo, *IEEE Transact. Geosci. Remote*, 51(3), 1393-1404, 10.1109/TGRS.2013.2243457, 2013.

Roujean, J.-L., M. Leroy, and P.-Y. Deschamps, A bidirectional reflectance model of the Earth's surface for the correction of remote sensing data, *J. Geophys. Res.,* 97(D18), 20455–20468, doi:10.1029/92JD01411, 1992.

Schmetz, J., P. Pili, S. Tjemkes, D. Just, J. Kerkmann, J., S. Rota, and A. Ratier, An introduction to Meteosat Second Generation (MSG). *Bull. Am. Meteorol. Soc.*, 83(7), 977-992, 2002.

Trigo, I. F., C. C. DaCamara, P. Viterbo, J.-L. Roujean, F. Olesen, C. Barroso, F. Camacho-de Coca, D. Carrer, S. C. Freitas, J. García-Haro, B. Geiger, F. Gellens-Meulenberghs, N. Ghilain, J. Meliá, L. Pessanha, N. Siljamo, and A. Arboleda, The Satellite Application Facility on Land Surface Analysis. *Int. J. Remote Sens.*, 32, 2725-2744, doi: 10.1080/01431161003743199, 2011.

Vermote, E. F., D. Tanre, J. L. Deuze, M. Herman, and J. J. Morcrette, Second simulation of the satellite signal in the solar spectrum, 6s: An overview. *IEEE T. Geosci. Remote*, 35(3), 675–686, 1997.

W. Wanner, X. Li, and A. H. Strahler, On the derivation of kernels for kernel-driven models of bidirectional reflectance, *J. Geophys. Res.,* **100**, 21,077 – 21,090, 1995.